International Journal of Nanomedicine

Dovepress
open access to scientific and medical research

Open Access Full Text Article

ORIGINAL RESEARCH

A New Pharmacokinetic Model Describing the Biodistribution of Intravenously and Intratumorally Administered Superparamagnetic Iron Oxide Nanoparticles (SPIONs) in a GL261 Xenograft Glioblastoma Model

This article was published in the following Dove Press journal:
International Journal of Nanomedicine

Alexander P Klapproth[1,2,*]
Maxim Shevtsov[1,3–7,*]
Stefan Stangl[1]
Wei Bo Li[2]
Gabriele Multhoff[1]

[1]Center for Translational Cancer Research Technische Universität München (TranslaTUM), Klinikum Rechts Der Isar, Munich, Germany; [2]Institute of Radiation Medicine, Helmholtz Zentrum München, German Research Center for Environmental Health (GmbH), Munich, Germany; [3]Institute of Cytology of the Russian Academy of Sciences (RAS), St. Petersburg, Russia; [4]Department of Biotechnology, First Pavlov State Medical University of St. Petersburg, St. Petersburg, Russia; [5]Almazov National Medical Research Centre, Russian Polenov Neurosurgical Institute, St. Petersburg, Russia; [6]National Center for Neurosurgery, Nur-Sultan, Kazakhstan; [7]Department of Biomedical Cell Technologies, Far Eastern Federal University, Vladivostok, Russia

*These authors contributed equally to this work

Background: Superparamagnetic iron oxide nanoparticles (SPIONs) have displayed multifunctional applications in cancer theranostics following systemic delivery. In an effort to increase the therapeutic potential of local therapies (including focal hyperthermia), nanoparticles can also be administered intratumorally. Therefore, the development of a reliable pharmacokinetic model for the prediction of nanoparticle distribution for both clinically relevant routes of delivery is of high importance.

Materials and Methods: The biodistribution of SPIONs (of two different sizes – 130 nm and 60 nm) radiolabeled with zirconium-89 or technetium-99m following intratumoral or intravenous injection was investigated in C57/Bl6 mice bearing subcutaneous GL261 glioblastomas. Based on PET/CT biodistribution data, a novel pharmacokinetic model was established for a better understanding of the pharmacokinetics of the SPIONs after both administration routes.

Results: The PET image analysis of the nanoparticles (confirmed by histology) demonstrated the presence of radiolabeled nanoparticles within the glioma site (with low amounts in the liver and spleen) at all investigated time points following intratumoral injection. The mathematical model confirmed the dynamic nanoparticle redistribution in the organism over a period of 72 h with an equilibrium reached after 100 h. Intravenous injection of nanoparticles demonstrated a different distribution pattern with a rapid particle retention in all organs (particularly in liver and spleen) and a subsequent slow release rate.

Conclusion: The mathematical model demonstrated good agreement with experimental data derived from tumor mouse models suggesting the value of this tool to predict the real-time pharmacokinetic features of SPIONs in vivo. In the future, it is planned to adapt our model to other nanoparticle formulations to more precisely describe their biodistribution in in vivo model systems.

Keywords: mathematical modeling, SPIONs, superparamagnetic iron oxide nanoparticles, pharmacokinetic model, glioblastoma, biodistribution

Background

Recent developments in nanotechnology have introduced novel diagnostic and therapeutic (ie, theranostic) applications of nanoparticles in translational and clinical oncology after intravenous injection.[1] Superparamagnetic iron oxide nanoparticles

Correspondence: Maxim Shevtsov; Wei Bo Li
Email maxim.shevtsov@tum.de; wli@helmholtz-muenchen.de

(SPIONs), specifically, have been identified as potential candidates for the development of innovative anti-tumor therapies due to their beneficial physico-chemical properties, biodistribution, biocompatibility and easy fabrication and functionalization.[2,3] Apart from intravenous injection, SPIONs can also be injected intratumorally to locally increase the temperature inside tumors after hyperthermia treatment.[4–7] Upon exposure to an external alternating magnetic field (AMF) and due to the Brownian and Néel relaxation and hysteresis loss, which is accompanied with the generation of thermal energy, a rise of the local tissue temperature up to 41–43 °C can be achieved.[8] Several studies reported the therapeutic potency of hyperthermia in preclinical models.[9–13] Apart from magnetic hyperthermia, other applications of functionalized SPIONs in translational oncology have been reported,[14] including the delivery of chemotherapeutic drugs, siRNA and small molecules.[3,14–19] In a recent study of our group SPIONs were decorated with the pro-apoptotic serine protease granzyme B (GrB-SPIONs). Administration of GrB-SPIONs resulted in significant delay of tumor progression and an increased overall survival in tumor-bearing animals.[3] Furthermore, the addition of photosensitizing agents to the composition of iron oxide nanoparticles enabled multimodal applications for both magnetic resonance imaging (MRI) and photothermal therapy.[20] In past decades, intravenous and intratumoral administrations of SPIONs have been extensively studied.[21–24] Compared to an intravenous injection mode, a local delivery of nanoparticles can significantly increase the concentrations of nanoparticles inside the tumor, while decreasing unfavorable off-target effects in healthy tissues.

The growing interest in nanoparticles as a vehicle for a targeted delivery of pharmaceutical agents have led to a vast increase in the development of novel physiologically based pharmacokinetic (PBPK) models.[25,26] These have been proven as valuable tools to simulate transportation kinetics of nanoparticles inside the body and to fill knowledge gaps for tissues that do not allow reliable measurements.[27] Several reviews have been published during the last decade summarizing the vast amount of novel PBPK models.[26,28–32] Partially responsible for the constant need of new and adjusted models is the large variability in pharmacokinetic behavior of nanoparticles differing in structural properties such as size, shape, material or coating compositions.[32] For choosing an appropriate model it is crucial to take into account not only biokinetic properties of the nanoparticles and the biological environment, but also the amount of available data. Many existing models split the circulating blood into two compartments, namely venous and arterial flux.[33–36] As measurements in most cases lack differentiation between these two compartments, the ratio between their respective concentrations can only be estimated. In practice, this is done either by fixing the ratio to a certain value, based on previous knowledge[33,36] or basically an additional degree of freedom for fitting the model parameters.[34,35] The latter should be avoided, when there are no reliable measurements available that validate the resulting ratio, as it rises the risk of overfitting. Therefore, in our model blood was treated as one compartment. An important factor present in the majority of PBPK models for nanoparticles[33–37] is the partition coefficient of blood and tissue which describes the ratio between concentration in a compartment and its outflow into the bloodstream.[38] However, due to the unique targeting properties of SPIONs in our experiment, we made the assumption that they do not accumulate within the tissue of organs, but enter the iron metabolism. This also reduces the degrees of freedom in the parameter estimation by omitting unnecessary features, bringing the model in line with the extent of available data.

In the present study, we have established a new pharmacokinetic model that mimics biological features of SPIONs after intratumoral or intravenous injection and prevents overfitting by focusing on predominant pathways specific to these nanoparticles. The model helps to understand the biodistribution of SPIONs over time and allows first predictions about their destiny inside the body after the two different injection routes.

Methods

Experiments

Superparamagnetic Iron Oxide Nanoparticles

The iron oxide dextran composite nanoparticles (Perimag®-COOH) with a hydrodynamic diameter of 130 nm and 60 nm were obtained from Micromod Partikeltechnologie GmbH. The zeta potential of nanoparticles characterized by electrophoretic measurements constituted –13.4 mV. The colloidal stability of these nanoparticles was analyzed for Perimag®-COOH formulations in H_2O distilled water, PBS buffer, and 5% human serum albumin (HSA) solution. Dynamic light scattering (DLS) measurements did not reveal any significant changes of the size distributions over a period of 3 months.

Before intratumoral or intravenous injection, particles were resuspended in PBS buffer (pH = 7.4).

Cells

Mouse GL261 glioblastoma cells were provided by Tumorbank Deutsches Krebsforschungszentrum (Heidelberg, Germany). Cells were cultured in RMPI-1640 medium supplemented with 10% fetal calf serum (FCS), 1 mM sodium pyruvate, 2 mM L-glutamine, and antibiotics (100 µg/mL streptomycin, 10 IU/mL penicillin) at 37 °C in 5% CO_2-incubator. For experiments, single-cell suspension was obtained employing Trypsin/0.53 mM EDTA.

Animals

Female, 8–10 weeks old C57Bl/6 mice were purchased from Charles River (Sulzfeld, Germany). All mice were kept and bred under specific pathogen-free conditions in accordance with the guidelines of the Federation of European Laboratory Science Association (FELASA). All animal experiments were performed in compliance with European Union law and approved by the ethical committee of First Pavlov State Medical University of St. Petersburg (St. Petersburg, Russia).

Glioblastoma Mouse Model

C57Bl/6 mice were anesthetized via i.p. injection of fentanyl 0.05 mg/kg, midazolam (5 mg/kg) and medetomidine (0.5 mg/kg). GL261 cells (5×10^6 cells suspended in 100 µL of phosphate-buffer solution) were injected into the right flank. After reaching a size of 50 mm^3, nanoparticles were injected either intravenously or intratumorally into the mice. Intravenous injection of nanoparticles was performed through the tail vein employing 0.3 mL insulin syringes (30 G) at a speed of 25 µL/min (total volume of injected solution constituted 200 µL). Intratumoral injections were performed using 0.3 mL insulin syringes (30 G) at a speed of 4 µL/min.

Radiolabeling of SPIONs with Zirconium-89 [^{89}Zr]

Radiolabeling of the nanoparticles with ^{89}Zr was performed as described previously.[39] Briefly, 35.6 MBq of Zirconium-89-oxalate ($^{89}Zr^{4+}$ in 1 M oxalic acid, PerkinElmer) was added to an Eppendorf tube with subsequent addition of Chelex-treated water (200 µL). The pH was raised to 8 employing 1 M Na_2CO_3 (aq.). Following addition of Chelex-36, treated water SPIONs Perimag®-COOH (400 µL, 50 mg Fe/mL) were added for the co-incubation period of 60 minutes at 100 °C. After cooling of the reaction to 22 °C, DTPA (50 µL, 10 mM (pH 7.5)) were added and left to stir at room temperature (for 30 minutes). The nanosuspension was purified employing size exclusion chromatography (SEC) (PD10 Sephadex, G25) and eluted with fractions of sterile PBS (recovery = 81%). Radiolabeled ^{89}Zr-Perimag®-COOH nanoparticles were diluted at a concentration of 20 mg Fe/mL employing sterile PBS with subsequent characterization using a nanosizer DLS (size constituted 134 ± 4.8 nm; Z-potential constituted −4.11 mV). Decay of ^{89}Zr was calculated employing www.radprocalculator.com/Decay.aspx with Gaussian filtering of 0.8.

PET/CT Imaging of Intratumorally Administered SPIONs

^{89}Zr-Perimag®-COOH solution (1.76 mg Fe/kg, 100 µL) was intravenously injected into the tail vein of the mice. PBS solution (100 µL) was used as control. In case of an intratumoral administration, nanoparticles were injected in an injection volume of 0.34 µL/mm^3 glioblastoma nodule. At designated time points animals were anesthetized with isoflurane (2% in O_2) and placed on a preheated bed (set at 38 °C) of the scanner. Whole body static PET scans were acquired employing nanoScan PET/CT (Mediso, Budapest, Hungary) with subsequent CT image acquisition. PET images were acquired employing 1–5 coincidence mode and recorded for 20 minutes. CT images were acquired at 300 ms exposure time in 720 projections with an acquisition time of 7 minutes employing a 50 kVp X-ray source. Subsequently, PET images were reconstructed by Tera-TomoTM 3D PET reconstruction software (Mediso version 2.01). Nucline software (Mediso version 2.01) was used to reconstruct CT images with a voxel size of 68 × 68 × 68 mm^3. VivoQuant software (InviCRO version 1.23patch3) was used for three-dimensional (3D) visualization and image analysis.

Biodistribution Analysis of the SPIONs

Animals under anesthesia employing Monastat Carter Multi-Channel Precision Pump (Barant Company, Montreal) were transcardially perfused with 0.1 M phosphate buffer (PB) to eliminate the blood from the tissues and organs. Briefly, following thoracotomy and exposure of the beating heart, perfusion tube was inserted into the left ventricle (another incision was performed in the right atrium) for perfusion of 200 mL of PB for 20 minutes. The obtained organ samples were employed for subsequent biodistribution analysis. Each tissue sample was weighed and counted employing a gamma counter (LKB compugamma for ^{99m}Tc studies, Wizard 2480 PerkinElmer for ^{89}Zr studies), together with standards prepared from

a sample of radiolabeled SPIONs. For each tissue type the percent of injected dose per gram (%ID/g) of tissue was calculated (after 24, 48 and 27 hours for intratumorally injected ^{89}Zr-Perimag®-COOH SPIONs; after 80 minutes and 24 hours for i.v. injected ^{89}Zr-Perimag®-COOH SPIONs; after 24 hours for i.v. injected ^{99m}Tc-ferucarbotran). To exclude the predominant accumulation of nanoparticles in macrophages at the tumor site the glioma sections were additionally stained for CD11b+ tumor-associated macrophages (TAMs) (Abcam, USA).

Pharmacokinetic Model

To describe the biodistribution of nanoparticles within mice after injection, a pharmacokinetic model was established. In this model the body is divided into distinct compartments (here: blood, organs and tumor), each describing a possible location of the investigated substance (here: SPIONs).

Model Structure

The transition between compartments is in this case described by linear, first-order ordinary differential equations with constant coefficients. Figure 1 shows the model structure and relation between different compartments. Equations (1–14) describe the change of the amount of SPIONs in each respective compartment as a function of time. The set of compartments is composed of blood and body parts, the latter including organs and the tumor. Blood is assumed to be the predominant way for transport of the nanoparticles between body parts. Therefore, the model differs from previous pharmacological models for both humans[40,41] and mice.[42–44] This systemic circulation (Figure 1B) is coupled with transport via the alimentary tract (Figure 1C).[45,46] Iron contained in in vivo administered SPIONs is predominantly included into the normal iron metabolism and therefore remains inside the body for a long-term period compared to other formulations of nanoparticles. Hence, excretion via urine was left out of the model. Each transition rate is described by one constant kinetic parameter $k_{i,j}$, with unit 1/t, as no saturation effects or delay are expected. Since the SPIONs were administered intratumorally, the initial values $S(0h)$ for each compartment other than the tumor were set to 0. As the data points were in the form of concentrations and normalized, the initial value for the tumor $S_{tumor}(0h)$ was set as $(w_{tumor} \cdot 100\%/g)$, with w_{tumor} denoting the mean tumor weight, which was presumed to be constant in the course of the experiment. The normalization of the data implies that 100% stands for the measurable dose released by the initially injected amount of SPIONs per gram tissue. The model is described by the following ordinary differential equations:

$$\dot{S}_{blood}(t) = \sum_{i=2}^{14} \left(k_{i,1} \cdot S_i(t) - k_{1,i} \cdot S_{blood}(t)\right) \quad (1)$$

$$\dot{S}_{tumor}(t) = -k_{2,1} \cdot S_{tumor}(t) + k_{1,2} \cdot S_{blood}(t) \quad (2)$$

$$\dot{S}_{liver}(t) = -k_{3,1} \cdot S_{liver}(t) + k_{1,3} \cdot S_{blood}(t) - k_{3,8} \cdot S_{liver}(t) \quad (3)$$

$$\dot{S}_{spleen}(t) = -k_{4,1} \cdot S_{spleen}(t) + k_{1,4} \cdot S_{blood}(t) \quad (4)$$

$$\dot{S}_{kidney}(t) = -k_{5,1} \cdot S_{kidney}(t) + k_{1,5} \cdot S_{blood}(t) \quad (5)$$

$$\dot{S}_{heart}(t) = -k_{6,1} \cdot S_{heart}(t) + k_{1,6} \cdot S_{blood}(t) \quad (6)$$

$$\dot{S}_{lung}(t) = -k_{7,1} \cdot S_{lung}(t) + k_{1,7} \cdot S_{blood}(t) \quad (7)$$

$$\dot{S}_{intestine}(t) = -k_{8,1} \cdot S_{intestine}(t) + k_{1,8} \cdot S_{blood}(t) + k_{3,8} \cdot S_{liver}(t) - k_{8,9} \cdot S_{intestine}(t) + k_{10,8} \cdot S_{stomach}(t) \quad (8)$$

$$\dot{S}_{colon}(t) = -k_{9,1} \cdot S_{colon}(t) + k_{1,9} \cdot S_{blood}(t) + k_{8,9} \cdot S_{intestine}(t) - k_{Exc} \cdot S_{colon}(t) \quad (9)$$

$$\dot{S}_{stomach}(t) = -k_{10,1} \cdot S_{stomach}(t) + k_{1,10} \cdot S_{blood}(t) - k_{10,8} \cdot S_{stomach}(t) \quad (10)$$

$$\dot{S}_{brain}(t) = -k_{11,1} \cdot S_{brain}(t) + k_{1,11} \cdot S_{blood}(t) \quad (11)$$

$$\dot{S}_{muscle}(t) = -k_{12,1} \cdot S_{muscle}(t) + k_{1,12} \cdot S_{blood}(t) \quad (12)$$

$$\dot{S}_{bone}(t) = -k_{13,1} \cdot S_{bone}(t) + k_{1,13} \cdot S_{blood}(t) \quad (13)$$

$$\dot{S}_{skin}(t) = -k_{14,1} \cdot S_{skin}(t) + k_{1,14} \cdot S_{blood}(t) \quad (14)$$

Parameter Estimation

Parameter estimation and simulations were performed in MATLAB. Ex vivo data with 3 different time points were used to estimate a set of optimal kinetic parameters, denoted by K. First, the measurements were converted from concentrations to data that are comparable in a pharmacokinetic model. For that, the experimental data points were multiplied by the mean weight

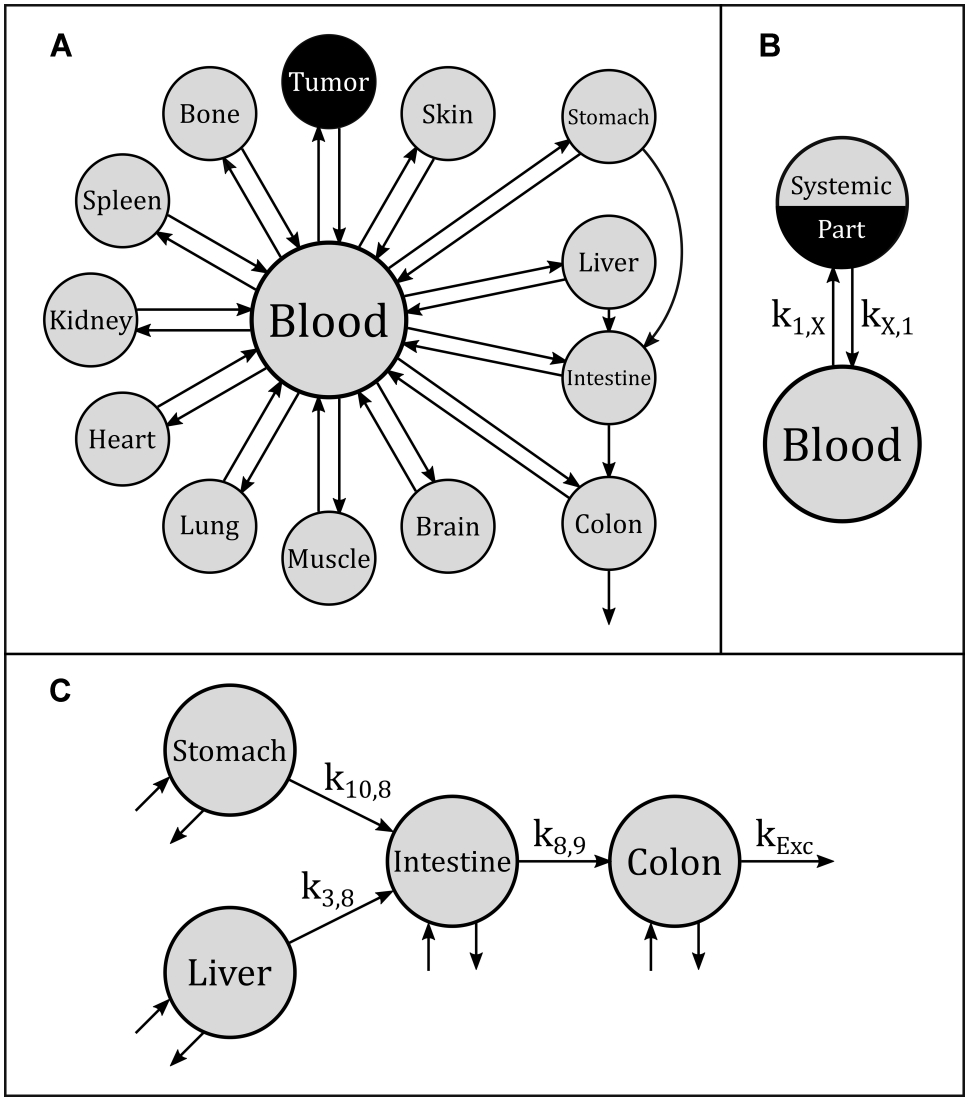

Figure 1 A mouse pharmacokinetic model for the kinetics of the biodistribution of SPIONs. (**A**) Overall model structure: Each bubble denotes one compartment and each arrow one pathway. The transition rate of each pathway $a \rightarrow b$ is described by one kinetic constant $k_{a,b}$. The intestine compartment represents the contents of the small intestine. (**B**) Systemic circulation: As blood is assumed to be the main transport mechanism between body parts, most pathways describe either the uptake rate constant from blood into a systemic part ($k_{1,X}$) or the emission rate constant from a systemic part into the blood ($k_{X,1}$). (**C**) Alimentary tract: Further transition parameters describe the pathways between organs that are part of the alimentary tract.

of the respective organs, which are described in literature.[42,47–52] The parameters were estimated in two steps, both employing a least squares objective function with added constraints and weights. First, the two parameters for each body part were approximated successively, starting with $k_{1,2}$ and $k_{2,1}$, followed by $k_{1,3}$ and $k_{3,1}$, etc. This was done by minimizing an individual objective function for each parameter pair with highly increased weights for said parameters. This was followed in the second step by a global multistart fit around the best values found during the first step and $N = 1000$. The objective function in this step had an added constraint that increases the function even further, if the observables are outside the confidence intervals of the experimental data points.

Results

In vivo Analysis of the Radiolabeled [^{89}Zr]-SPION Biodistribution

In order to quantify the retention of intratumorally administered SPIONs within GL261 glioblastoma, systemic biodistribution studies were performed, utilizing ^{89}Zr-labeled SPIONs. Nanoparticles were injected intratumorally in a volume of 0.34 µL/mm^3. Treated mice were subsequently imaged using PET-CT at 1, 24, 48 and 72 h following

injection (n = 4). The image analysis of a single animal at all time points clearly demonstrated the localization of the signal within the tumor site or around the injection canal at all time points. Subsequent Prussian blue staining was performed to confirm the presence of iron oxide nanoparticles inside tumor cells (cf. Supplementary Figure S1).

Following injection of the SPIONs ex vivo organ counting was performed at 24, 48 and 72 h (n = 3 per group). The analysis proved that the majority of the injected nanoparticles were present either within the skin and adjunctive tissue of the tumor or within the glioblastoma. Additionally, uptake was observed in the liver, which is indicative for transport of the nanoparticles via blood circulation to this organ. Subsequent estimation of the ID across all time points demonstrated that nearly 50% of the ID accumulated with the glioblastoma (21–87%, n = 9). At the end of the follow-up period at 72 h 46% of the ID was retained in the tumor site (36–57%, n = 3). The precise comparison of the tumor to tissue ratio indicated an over 50-fold increase in nanoparticle retention in the tumor tissue compared to other tissues.

Pharmacokinetic Model

The mathematical model was established as a dynamical system (ie, changing over time) of distinct compartments, each containing a certain amount of ^{89}Zr-Perimag®-COOH SPIONs at each point in time (cf. Figure 1). This amount was measured using a gamma counter and normalized. The initial amount of injected SPIONs $S_{tumor}(0h)$ was indicated as 100% per g and the measured values accordingly as percentages per g. To have comparable numbers in regard to a pharmacokinetic model these values were each multiplied by the respective mean organ weight derived from literature.[42,47-52]

Intratumorally Injected SPIONs

The developed pharmacokinetic model was used to estimate optimal kinetic parameters that best describe the measured data. The set of estimated parameters, denoted by K, can be found in Table 1.

The kinetic parameters contained in K were used for simulations, starting from initial values $S(0h)$. As shown in Figure 2, the simulations fit the measurements very well, except for body parts with very low values and too much background noise. Due to the intratumoral injection, all SPIONs are located inside the tumor at $t = 0$. According to both experimental data and simulations, a rapid release of SPIONs from the tumor occurs within the first 30 min after intratumoral injection. After 30 min the release of nanoparticles from the tumor steadily decreases. Nanoparticles released from the tumor also accumulate rapidly in other organs within the first 30 min. Then the uptake slows down during the following 100 h until an equilibrium is reached, with a certain amount of SPIONs retained in every compartment (cf. Supplementary Figure S2). In contrast, liver and spleen show a steady, low uptake of the nanoparticles over the whole period of time according to the model. Liver and spleen are therefore the major destiny of SPIONs. These results are confirmed by recent findings of other groups.[53–55]

Table 1 Computed Kinetic Parameters (K). Each Value in the Upper Part Describes the Rate Constant of Either the Uptake of SPIONs into a Body Part from Blood or the Emission from a Body Part into Blood. The Values in the Lower Part Each Describe One Rate Constant of the Alimentary Tract. The Unit of Each Constant Is 1/h

Body Part	Uptake Rate ($k_{1,X}$)	Emission Rate ($k_{X,1}$)
Tumor	327.4	40.06
Liver	0.1159	$5.067 \cdot 10^{-4}$
Spleen	$9.780 \cdot 10^{-4}$	$1.409 \cdot 10^{-5}$
Kidney	3.804	15.66
Colon	0.7151	689.6
Stomach	7.411	896.0
Lung	1.903	148.5
Small Intestine	68.93	59.41
Muscle	194.2	62.39
Bone	62.60	38.58
Skin	9.380	27.58
Brain	5.439	795.6
Heart	2.416	490.5
Pathway	**Notation**	**Rate**
Liver → Sm. Intest.	$k_{3,8}$	$4.947 \cdot 10^{-4}$
Stomach → Sm. Intest.	$k_{10,8}$	64.71
Sm. Intest. → Colon	$k_{8,9}$	3.447
Colon → Excretion	k_{Exc}	$4.244 \cdot 10^{-3}$

Intravenously Injected SPIONs

To further validate the model two data sets from mice with intravenously injected SPIONs were analyzed.[39] The experimental data of both experiments could be described very well with the pharmacokinetic model (cf. Figure 3). The first set of data resulted from biodistribution studies with ^{99m}Tc-ferucarbotran injected into the tail vein of GL261 tumor bearing C57BL/6 mice. Although no data were available for the

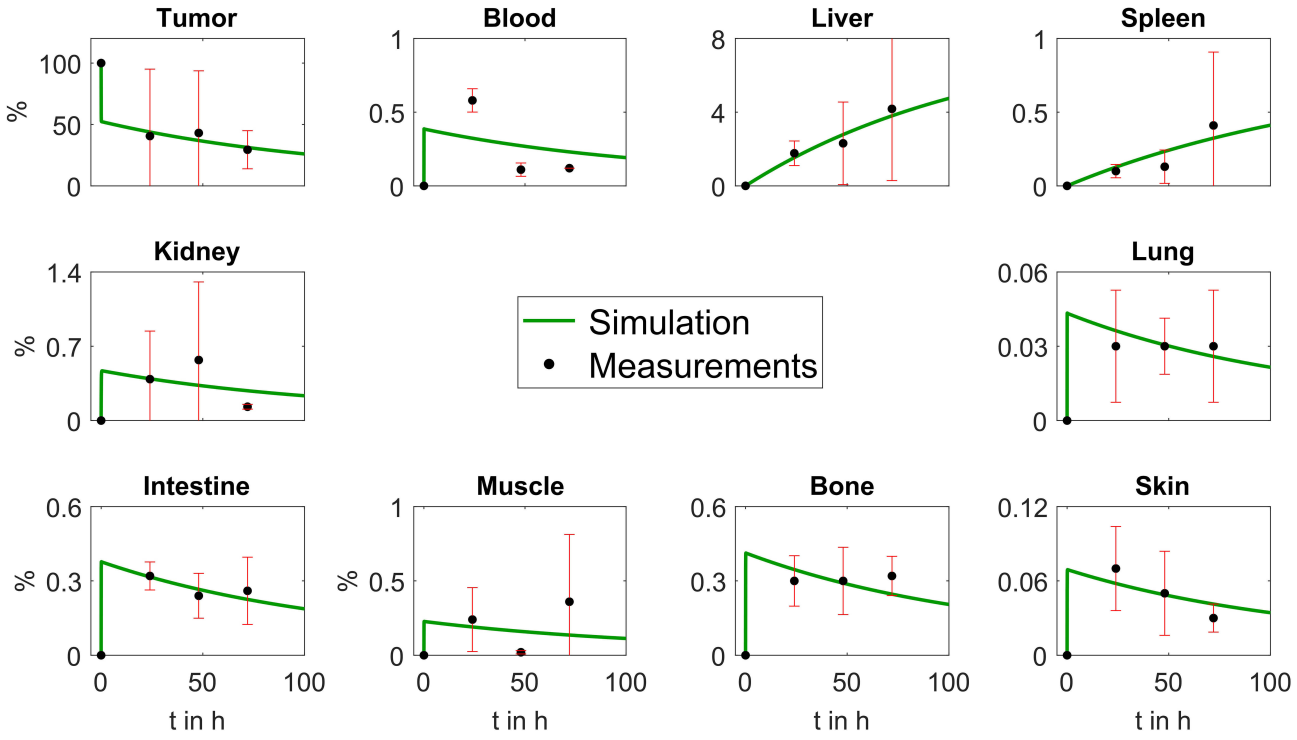

Figure 2 Plots depicting comparative analysis of ex vivo biodistribution data from intratumorally injected ^{89}Zr-Perimag®-COOH and simulation results calculated by our mathematical model. Each plot shows the results for one compartment. The black dots represent the mean values of the measured biodistribution data at a single time point and the red bars their standard deviation. The green curves depict the outcome of the simulations using the mathematical model and the set of estimated kinetic parameters K. All x-axes run from 0 to 100 h. The y-axes represent percentages of the released dose per gram of the initially injected amount of SPIONs. "Intestine" represents the contents of the small intestine. The respective plots for heart, colon, stomach and brain were below 0.005% at each time point (data not shown).

amount of SPIONs inside the skin, the previous uptake parameters from K for the skin could be used to make predictions. The parameters for the organs with available measurements were estimated anew by a parameter fit using the measurements (cf. Supplementary Table S1).

A similar analysis was performed on data from studies using ^{89}Zr-Perimag®-COOH nanoparticles (130 nm) that were injected into the tail vein of tumor-free C57BL/6 mice. Biodistribution data were acquired 80 min and 24 h after injection. As there was no data available for heart and skin, the already found parameters were again adopted from K to make predictions for the uptake inside these body parts (cf. Supplementary Table S2). The data for the other organs could be described very well with our pharmacokinetic model (cf. Figure 4).

Comparing the plots in Figures 3 and 4 shows that the progression of the curves is very similar for most organs with the exception of spleen and bone. The data points for the spleen in Figure 4 are very similar, which suggests a rapid increase within 80 min, when the amount inside the spleen has already reached its equilibrium. In Figure 3, however, the model predicts a slower increase of nanoparticles inside the spleen. The difference in the bone curves is due to the fact that the uptake of ^{89}Zr-Perimag®-COOH nanoparticles persists from 80 min to 24 h, whereas that of ^{99m}Tc-ferucarbotran nanoparticles further increases after 24 h.

There are also notable differences between the curve progressions of the plots from intratumoral injection data and intravenous injection data. These can be explained by the huge and rapid decrease in blood after i.v. injection compared to the relatively slow decrease inside the tumor tissue after intratumoral injection. While for the latter the increase in most other organs is also very fast in the beginning, the increase stops, when a more stable state is reached. Thereafter, a slow transport of SPIONs into liver and spleen from all other organs occurs. After i.v. injection, however, the SPIONs are rapidly emitted into all organs, causing a short peak inside most of them, before most nanoparticles are immediately transported into organs with higher retention capacity. Also notable is that after i.v. injection the liver directly absorbs a large amount of SPIONs, whereas the increase is much slower, yet more steady and lasting after intratumoral injection.

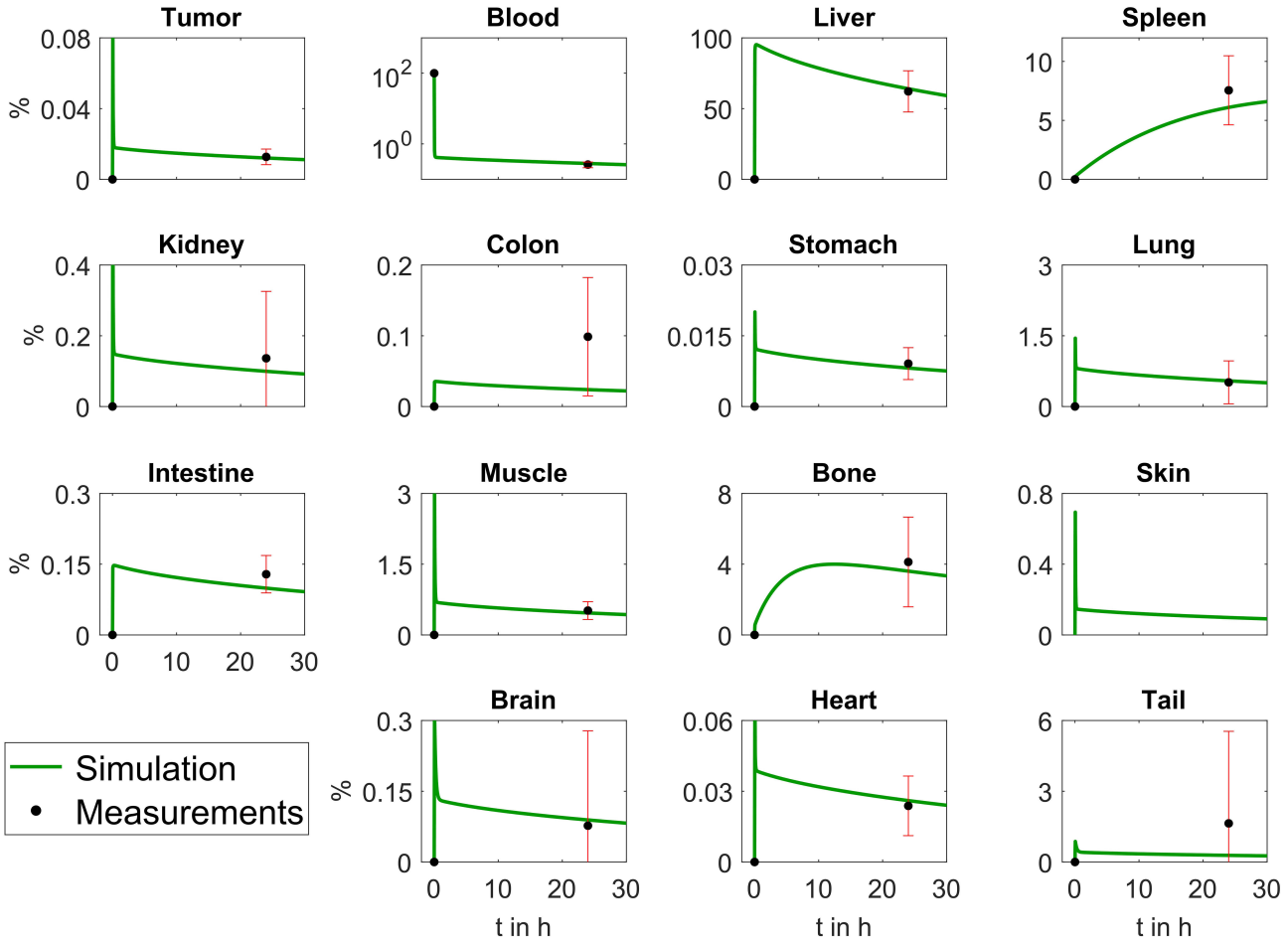

Figure 3 Plots depicting comparative analysis of ex vivo biodistribution data from i.v. injected ^{99m}Tc-ferucarbotran and simulation results. The black dots represent the mean values of the measured biodistribution data at $t =$ 24 h and the red lines their respective error bars. The green curves depict the outcome of the simulations using the mathematical model. All x-axes run from 0 to 30 h.

Discussion

Applications of nanotechnology have enabled the development of anti-cancer diagnostic and therapeutic agents that provided promising results for translational and clinical oncology.[56–58] One possible route for the administration of nanoparticles is the intratumoral injection, which can provide (i) a high local concentration of the agent, (ii) reduction of the particle clearance (ie, renal or hepatic clearance) that increases the bioavailability of nanoparticles, (iii) decrease in the off-target side effects, and (iv) avoidance of the natural histo-hematic barriers (eg, brain-blood barrier). In the current study, we analyzed the biodistribution of intratumorally injected SPIONs into brain tumors for which we developed a new mathematical model for prediction of particle clearance from the injection site. We observed a predominant retention (46% of the ID) of the radiolabeled ^{89}Zr-Perimag®-COOH in the GL261 glioblastoma over a period of 72 h. To show a potential localization of nanoparticles in tumor-associated macrophages the glioma sections were stained for CD11b, which is a marker for TAMs. Only very few CD11b+ TAMs were found with intracellular localized nanoparticles in a field of view (×20) inside the tumor (data not shown). These data indicate that most nanoparticles are taken up by tumor cells and not by CD11b+ TAMs. Intriguingly, some uptake of the SPIONs was observed within the liver and spleen tissues at 48 and 72 h post-injection. Presumably, these nanoparticles reached these tissues via the blood circulation. The main limitation of the implemented non-orthotopic tumor mouse model is the elimination of the brain-blood barrier (BBB) that could hamper the delivery of theranostic agents to the glioma site in the brain. However, the applied dose of the intratumorally administered nanoparticles (ie, 0.34 µg/mm^3) was too high for an orthotopic glioblastoma model. The large volume would result in intracranial hypertension with subsequent brain dislocation. To avoid these

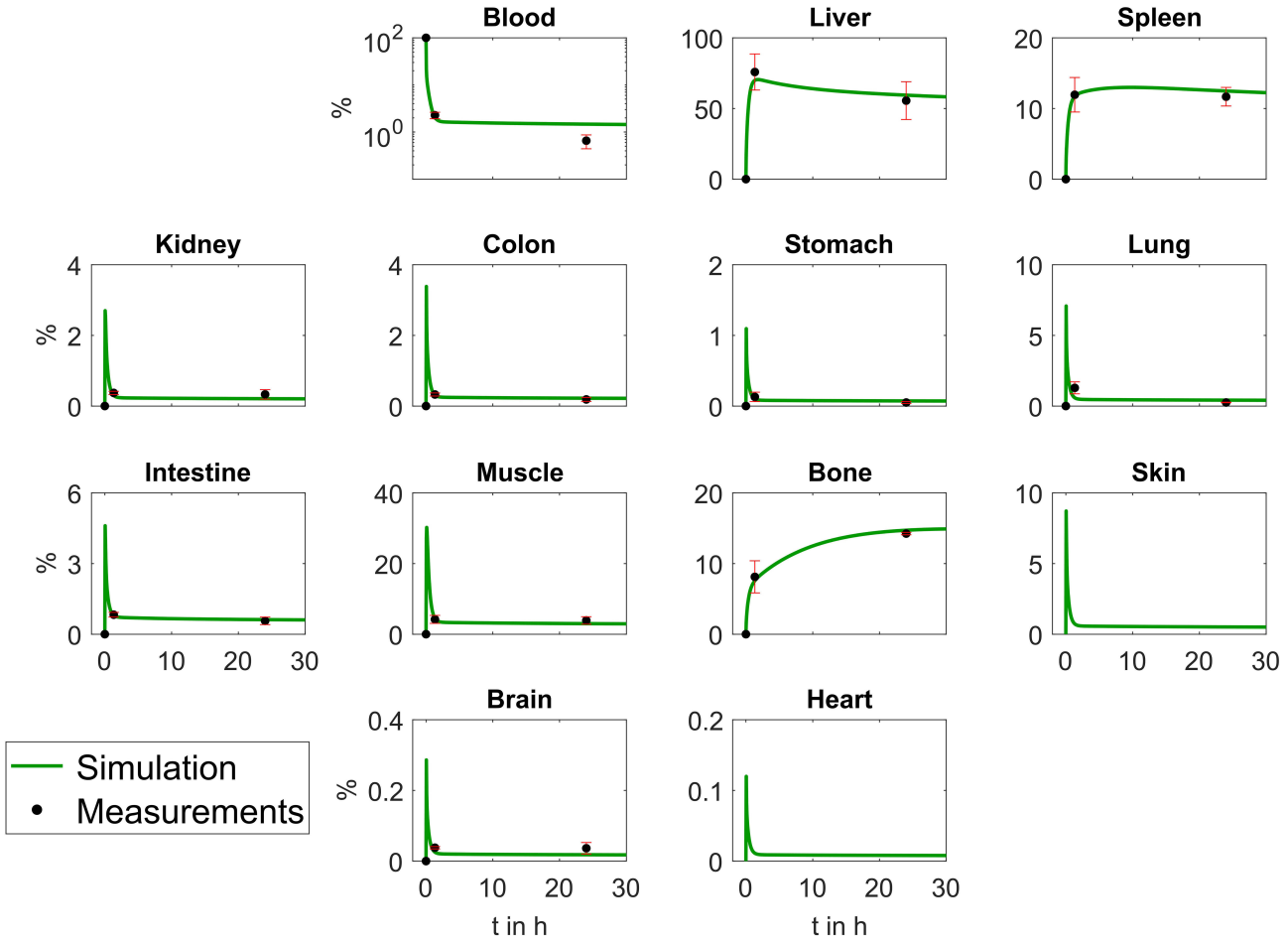

Figure 4 Plots depicting comparative analysis of ex vivo biodistribution data from i.v. injected ^{89}Zr-Perimag®-COOH and simulation results. The black dots represent the mean values of the measured biodistribution data at $t = 24$ h and the red lines their respective standard deviation. The green curves depict the outcome of the simulations using the mathematical model. All x-axes run from 0 to 30 h.

complications our modeling experiments were performed in GL261 tumors which were implanted into the flank of the mice.

The obtained data of the pharmacokinetics of the labeled nanoparticles are in line with previously published in vivo data on the biodistribution of locally injected nanoparticles of various formulations.[59–61] Xie et al reported the biodistribution of intratumorally infused copper-64 (^{64}Cu) nanoshells labelled with radionuclide in the head and neck squamous cell carcinoma xenograft in nude mice.[61] Employing positron emission tomography/computer tomography (PET/CT) imaging the authors demonstrated higher retention of ^{64}Cu nanoshells for a period of 44 h post-injection inside the tumor with low concentrations in healthy tissues.[61] In another study by Chi et al intratumorally injected ^{131}I gelatin microspheres (^{131}I-GMSs) remained in human hepatocellular carcinoma (HepG2) of nude Balb/c mice for a period of 32 days and resulted in a suppressed tumor growth and an increased overall survival.[59] To increase the accuracy of the magnetic nanoparticle imaging novel, highly sensitive technologies, particularly magnetic particles imaging (MPI), are necessary for the detection of nanoparticles at very low concentrations (2 pg per cell).[4–6]

In line with the in vivo biodistribution studies, the developed mathematical model allowed us to predict the behavior of SPIONs after intratumoral and intravenous injection (cf. Figure 2). However, certain limitations should be kept in mind, when employing this model. Weights of all body parts were assumed to be equal for all mice. Particularly the tumor weight may differ vastly between different groups of animals and information about the tumor size is an important part of adjustments of parameters in the model. A suggestion for further studies would therefore be to estimate the parameters separately for each test subject and perform a statistical analysis on the comparability of the resulting parameters. Differences

between measurement points in compartments with unsatisfactory fits can be explained by substantial noise or other uncertainties. Adding multiple parameters to the affected parameters to increase the quality of the fits may result in overfitting and incorrect conclusions. The parameters were estimated by comparing simulated observables with the means of the experimental data points, while employing an additional penalty constraint for observables outside the confidence intervals of the data. The initial values for each fit were chosen randomly around previously found values. Multistart sampling like this has been proven to be very effective for modeling complex biological systems.[62] More advanced models that take specific biomechanical features of the compartments into account are planned, when more experimental data are available.

Long-term local deposition and low clearance of nanoparticles could be employed for the prolonged local antitumor therapies that could include hyperthermia treatment, chemo/radiotherapy or a combination of these therapeutic modalities. Indeed, several studies reported on improved tumor outcome after locally delivered nanoparticle-based agents.[60,63-67] Thus, in the recent study by Li et al intratumorally injected MnS@Bi_2S_3-PEG nanoparticles in combination with hyperthermia treatment significantly boosted the efficacy of radiotherapy, indicating the synergistic anti-tumor effect.[64]

The properties that are known to affect the biodistribution and clearance of nanoparticles include the size, chemical composition, surface charge and chemistry and shape.[68] The main limitation of the current study is that for our mathematical modeling SPIONs with a diameter of ≈ 130 nm were used. Though the developed pharmacokinetic model could describe the behavior of nanoparticles of this size, the computed parameters are very likely to differ for other sizes of nanoparticles or mouse models. To test the impact of the size of the nanoparticles on the mathematical model ^{99m}Tc-ferucarbotran-labeled nanoparticles with a diameter of approximately 60 nm were used for i.v. administration. As expected, the analysis of these data sets showed that even though the mathematical model is applicable also for intravenous injection, the parameters differed strongly for ^{99m}Tc-ferucarbotran nanoparticles with a size of 60 nm after i.v. injection into C57BL/6 mice. Due to the smaller size, these nanoparticles are taken up and metabolized through different pathways compared to larger nanoparticles. To investigate if these changes are due to differences in SPION characteristics or mouse models, further studies are necessary. Although the assumptions allow the application of the model for other iron oxide nanoparticles, the process of parameter estimation should be repeated in studies involving nanoparticles with different biochemical and biophysical properties.

The analysis of the data from intravenously administered SPIONs showed that at least without targeting the number of particles reaching the tumor is surely below the desired amount. The model predicts that immediately after injection the dose inside the tumor peaks at around 0.07% of the initially injected dose. After that most of the nanoparticles are transported to liver and spleen. In comparison, after intratumoral injection around 80% of the initial dose stays inside the tumor for more than two days. To raise the peak after i.v. injection to the same scale, the overall injected dose would have to be increased by at least a three-digit factor. Such a concentration would be toxic for other organs like liver and spleen, which would suffer from an increased uptake by the same factor, and is therefore not possible. To overcome this problem one could employ functionalized targeting nanoparticles with an improved accumulation inside the tumor. Previously, several studies reported the enhanced accumulation of functionalized tumor-targeted nanoparticles as compared to non-coated particles.[16,69,70] The effect of tumor targeting on biodistribution both biologically and mathematically will hence be the next important step in further studies, since ways to make intravenous injections viable may be a crucial part of making nanoparticle-based agents viable for clinical application.

In conclusion, the developed pharmacokinetic model is applicable for biodistribution studies on iron oxide nanoparticles. As Henrique Silva et al already indicated, pharmacokinetic models provide a valuable tool in understanding the biodistribution of SPIONs.[53] In this case, the common structure of PBPK models was reduced to only predominant pathways to predict meaningful results for the available experimental data sets. This enables applications of the model to in vivo studies on SPIONs for further experimental investigations, where collecting large amounts of time dependent data is usually difficult. Yet it is important to regard the potentially large effects of changes in nanoparticle properties on biological behavior, which are likely to result in specific kinetic transfer parameters for each type of nanoparticle. Further experimental investigations of SPIONs in mice and humans can provide additional pharmacokinetic data and

may provide insights into biochemical and physiological processes of nanoparticles in organs and tumors, possibly even on a cellular level. This can further improve the model structure and the transfer coefficients. The pharmacokinetic model developed in this study can be further modified by employing available experimental data and adapted to describe the kinetic processes of other therapeutic nanoparticles, such as gold nanoparticles in in vivo xenograft model.

Acknowledgments

The study was supported by the Russian Foundation for Basic Research (RFBR) according to the research project № 20-38-70039 and DFG grant (SFB824/3, STA1520/1-1), Technische Universität München (TUM) within the DFG funding program Open Access Publishing. Additional financial support was provided by TaGoNaX DFG project № 336532926.

Disclosure

The authors declare no conflict of interest. The funders had no role in the design of the study; in the collection, analyses, or interpretation of data; in the writing of the manuscript, or in the decision to publish the results.

References

1. Jahangirian H, Kalantari K, Izadiyan Z, Rafiee-Moghaddam R, Shameli K, Webster TJ. A review of small molecules and drug delivery applications using gold and iron nanoparticles. *Int J Nanomedicine*. 2019;14:1633–1657. doi:10.2147/IJN.S184723
2. Shevtsov M, Multhoff G. Recent developments of magnetic nanoparticles for theranostics of brain tumor. *Curr Drug Metab*. 2016;17(8):737–744. doi:10.2174/1389200217666160607232540
3. Shevtsov M, Stangl S, Nikolaev B, et al. Granzyme B functionalized nanoparticles targeting membrane Hsp70-positive tumors for multimodal cancer theranostics. *Small*. 2019;15(13):e1900205. doi:10.1002/smll.201900205
4. Abed Z, Beik J, Laurent S, et al. Iron oxide-gold core-shell nanotheranostic for magnetically targeted photothermal therapy under magnetic resonance imaging guidance. *J Cancer Res Clin Oncol*. 2019;145(5):1213–1219. doi:10.1007/s00432-019-02870-x
5. Asadi M, Beik J, Hashemian R, et al. MRI-based numerical modeling strategy for simulation and treatment planning of nanoparticle-assisted photothermal therapy. *Phys Med*. 2019;66:124–132. doi:10.1016/j.ejmp.2019.10.002
6. Beik J, Asadi M, Khoei S, et al. Simulation-guided photothermal therapy using MRI-traceable iron oxide-gold nanoparticle. *J Photochem Photobiol B*. 2019;199:111599. doi:10.1016/j.jphotobiol.2019.111599
7. Janko C, Ratschker T, Nguyen K, et al. Functionalized superparamagnetic iron oxide nanoparticles (SPIONs) as platform for the targeted multimodal tumor therapy. *Front Oncol*. 2019;9:59. doi:10.3389/fonc.2019.00059
8. Deatsch AE, Evans BA. Heating efficiency in magnetic nanoparticle hyperthermia. *J Magn Magn Mater*. 2014;354:163–172. doi:10.1016/j.jmmm.2013.11.006
9. Chao Y, Chen G, Liang C, et al. Iron nanoparticles for low-power local magnetic hyperthermia in combination with immune checkpoint blockade for systemic antitumor therapy. *Nano Lett*. 2019;19(7):4287–4296–4287–4296. doi:10.1021/acs.nanolett.9b00579
10. Jordan A, Scholz R, Maier-Hauff K, et al. The effect of thermotherapy using magnetic nanoparticles on rat malignant glioma. *J Neurooncol*. 2006;78(1):7–14. doi:10.1007/s11060-005-9059-z
11. Popescu RC, Andronescu E, Grumezescu AM. In vivo evaluation of Fe(3)O(4) nanoparticles. *Rom J Morphol Embryol*. 2014;55(3 Suppl):1013–1018.
12. Wang R, Chen C, Yang W, Shi S, Wang C, Chen J. Enhancement effect of cytotoxicity response of silver nanoparticles combined with thermotherapy on C6 rat glioma cells. *J Nanosci Nanotechnol*. 2013;13(6):3851–3854. doi:10.1166/jnn.2013.7156
13. Yi GQ, Gu B, Chen LK. The safety and efficacy of magnetic nano-iron hyperthermia therapy on rat brain glioma. *Tumour Biol*. 2014;35(3):2445–2449. doi:10.1007/s13277-013-1324-8
14. Mukherjee S, Liang L, Veiseh O. Recent advancements of magnetic nanomaterials in cancer therapy. *Pharmaceutics*. 2020;12(2):147. doi:10.3390/pharmaceutics12020147
15. Choi KY, Liu G, Lee S, Chen X. Theranostic nanoplatforms for simultaneous cancer imaging and therapy: current approaches and future perspectives. *Nanoscale*. 2012;4(2):330–342. doi:10.1039/C1NR11277E
16. Hadjipanayis CG, Machaidze R, Kaluzova M, et al. EGFRvIII antibody-conjugated iron oxide nanoparticles for magnetic resonance imaging-guided convection-enhanced delivery and targeted therapy of glioblastoma. *Cancer Res*. 2010;70(15):6303–6312. doi:10.1158/0008-5472.CAN-10-1022
17. Schleich N, Sibret P, Danhier P, et al. Dual anticancer drug/superparamagnetic iron oxide-loaded PLGA-based nanoparticles for cancer therapy and magnetic resonance imaging. *Int J Pharm*. 2013;447(1–2):94–101. doi:10.1016/j.ijpharm.2013.02.042
18. Zhu L, Zhou Z, Mao H, Yang L. Magnetic nanoparticles for precision oncology: theranostic magnetic iron oxide nanoparticles for image-guided and targeted cancer therapy. *Nanomedicine (Lond)*. 2017;12(1):73–87. doi:10.2217/nnm-2016-0316
19. Xing R, Bhirde AA, Wang S, et al. Hollow iron oxide nanoparticles as multidrug resistant drug delivery and imaging vehicles. *Nano Res*. 2012;6(1):1–9. doi:10.1007/s12274-012-0275-5
20. Zhou Z, Sun Y, Shen J, et al. Iron/iron oxide core/shell nanoparticles for magnetic targeting MRI and near-infrared photothermal therapy. *Biomaterials*. 2014;35(26):7470–7478. doi:10.1016/j.biomaterials.2014.04.063
21. Giustini AJ, Ivkov R, Hoopes PJ. Magnetic nanoparticle biodistribution following intratumoral administration. *Nanotechnology*. 2011;22(34):345101. doi:10.1088/0957-4484/22/34/345101
22. Gultepe E, Reynoso FJ, Jhaveri A, et al. Monitoring of magnetic targeting to tumor vasculature through MRI and biodistribution. *Nanomedicine (Lond)*. 2010;5(8):1173–1182. doi:10.2217/nnm.10.84
23. Natarajan A, Gruettner C, Ivkov R, et al. NanoFerrite particle based radioimmunonanoparticles: binding affinity and in vivo pharmacokinetics. *Bioconjug Chem*. 2008;19(6):1211–1218. doi:10.1021/bc800015n
24. Shevtsov MA, Nikolaev BP, Ryzhov VA, et al. Brain tumor magnetic targeting and biodistribution of superparamagnetic iron oxide nanoparticles linked with 70-kDa heat shock protein study by nonlinear longitudinal response. *J Magn Magn Mater*. 2015;388:123–134. doi:10.1016/j.jmmm.2015.04.030
25. Jacquez JA. Compartmental analysis in biology and medicine. *BioMedware*. 1996.
26. Li M, Zou P, Tyner K, Lee S. Physiologically based pharmacokinetic (PBPK) modeling of pharmaceutical nanoparticles. *AAPS J*. 2017;19(1):26–42. doi:10.1208/s12248-016-0010-3
27. Hagens WI, Oomen AG, de Jong WH, Cassee FR, Sips AJ. What do we (need to) know about the kinetic properties of nanoparticles in the body? *Regul Toxicol Pharmacol*. 2007;49(3):217–229. doi:10.1016/j.yrtph.2007.07.006

28. Li M, Al-Jamal KT, Kostarelos K, Reineke J. Physiologically based pharmacokinetic modeling of nanoparticles. *ACS Nano*. 2010;4(11):6303–6317. doi:10.1021/nn1018818
29. Sager JE, Yu J, Ragueneau-Majlessi I, Isoherranen N. Physiologically based pharmacokinetic (PBPK) modeling and simulation approaches: a systematic review of published models, applications, and model verification. *Drug Metab Dispos*. 2015;43(11):1823–1837. doi:10.1124/dmd.115.065920
30. Yellepeddi V, Rower J, Liu X, Kumar S, Rashid J, Sherwin CMT. State-of-the-art review on physiologically based pharmacokinetic modeling in pediatric drug development. *Clin Pharmacokinet*. 2019;58(1):1–13. doi:10.1007/s40262-018-0677-y
31. Yoshida K, Budha N, Jin JY. Impact of physiologically based pharmacokinetic models on regulatory reviews and product labels: frequent utilization in the field of oncology. *Clin Pharmacol Ther*. 2017;101(5):597–602. doi:10.1002/cpt.622
32. Yuan D, He H, Wu Y, Fan J, Cao Y. Physiologically based pharmacokinetic modeling of nanoparticles. *J Pharm Sci*. 2019;108(1):58–72. doi:10.1016/j.xphs.2018.10.037
33. Carlander U, Li D, Jolliet O, Emond C, Johanson G. Toward a general physiologically-based pharmacokinetic model for intravenously injected nanoparticles. *Int J Nanomedicine*. 2016;11:625–640. doi:10.2147/IJN.S94370
34. Li D, Morishita M, Wagner JG, et al. In vivo biodistribution and physiologically based pharmacokinetic modeling of inhaled fresh and aged cerium oxide nanoparticles in rats. *Part Fibre Toxicol*. 2016;13(1):45. doi:10.1186/s12989-016-0156-2
35. Li M, Panagi Z, Avgoustakis K, Reineke J. Physiologically based pharmacokinetic modeling of PLGA nanoparticles with varied mPEG content. *Int J Nanomedicine*. 2012;7:1345–1356. doi:10.2147/IJN.S23758
36. Sweeney LM, MacCalman L, Haber LT, Kuempel ED, Tran CL. Bayesian evaluation of a physiologically-based pharmacokinetic (PBPK) model of long-term kinetics of metal nanoparticles in rats. *Regul Toxicol Pharmacol*. 2015;73(1):151–163. doi:10.1016/j.yrtph.2015.06.019
37. Péry ARR, Brochot C, Hoet PHM, Nemmar A, Bois FY. Development of a physiologically based kinetic model for 99m-Technetium-labelled carbon nanoparticles inhaled by humans. *Inhal Toxicol*. 2009;21(13):1099–1107. doi:10.3109/08958370902748542
38. Kousba A, Sultatos LG. Continuous system modeling of equilibrium dialysis for determinations of tissue partitioning of parathion and paraoxon. *Toxicol Lett*. 2002;133(2):153–159. doi:10.1016/S0378-4274(02)00131-5
39. Abdollah MRA, Carter TJ, Jones C, et al. Fucoidan prolongs the circulation time of dextran-coated iron oxide nanoparticles. *ACS Nano*. 2018;12(2):1156–1169. doi:10.1021/acsnano.7b06734
40. Li WB, Höllriegl V, Roth P, Oeh U. Influence of human biokinetics of strontium on internal ingestion dose of 90Sr and absorbed dose of 89Sr to organs and metastases. *Radiat Environ Biophys*. 2008;47(2):225–239. doi:10.1007/s00411-007-0154-8
41. Human alimentary tract model for radiological protection. ICRP Publication 100. *Ann ICRP*. 2006;36(1–2):25–30. doi:10.1016/j.icrp.2006.03.004
42. Baxter LT, Zhu H, Mackensen DG, Jain RK. Physiologically based pharmacokinetic model for specific and nonspecific monoclonal antibodies and fragments in normal tissues and human tumor xenografts in nude mice. *Cancer Res*. 1994;54(6):1517–1528.
43. Garg A, Balthasar JP. Physiologically-based pharmacokinetic (PBPK) model to predict IgG tissue kinetics in wild-type and FcRn-knockout mice. *J Pharmacokinet Pharmacodyn*. 2007;34(5):687–709. doi:10.1007/s10928-007-9065-1
44. Polli JR, Engler FA, Balthasar JP. Physiologically based modeling of the pharmacokinetics of "catch-and-release" anti-carcinoembryonic antigen monoclonal antibodies in colorectal cancer xenograft mouse models. *J Pharm Sci*. 2019;108(1):674–691. doi:10.1016/j.xphs.2018.09.037
45. Guyton AC, Hall JE. *Textbook of Medical Physiology*. Philadelphia, PA: Elsevier Sanders; 2006.
46. Paquet F, Bailey MR, Leggett RW; on Radiological Protection IC. Occupational intakes of radionuclides: part 2. ICRP publication 134. *Ann ICRP*. 2016;45(3–4):7–349. doi:10.1177/0146645316670045
47. Bigham ML, Cockrem F. Body weights, tail lengths, body temperatures, food intakes, & some slaughter data for four strains of mice reared at three different environmental temperatures. *New Zeal J Agri Res*. 2012;12(4):658–668. doi:10.1080/00288233.1969.10421217
48. Konarzewski M, Diamond J. Evolution of basal metabolic rate and organ masses in laboratory mice. *Evolution*. 1995;49(6):1239–1248. doi:10.1111/j.1558-5646.1995.tb04450.x
49. Kumral A, Tugyan K, Gonenc S, et al. Protective effects of erythropoietin against ethanol-induced apoptotic neurodegenaration and oxidative stress in the developing C57BL/6 mouse brain. *Brain Res Dev Brain Res*. 2005;160(2):146–156. doi:10.1016/j.devbrainres.2005.08.006
50. Riches AC, Sharp JG, Thomas DB, Smith SV. Blood volume determination in the mouse. *J Physiol*. 1973;228(2):279–284. doi:10.1113/jphysiol.1973.sp010086
51. Wang Q, Sun P, Li G, Zhu K, Wang C, Zhao X. Inhibitory effects of Dendrobium candidum Wall ex Lindl. on azoxymethane- and dextran sulfate sodium-induced colon carcinogenesis in C57BL/6 mice. *Oncol Lett*. 2014;7(2):493–498. doi:10.3892/ol.2013.1728
52. Xiao F, Furuta T, Takashima M, Shirai N, Hanai H. Involvement of cyclooxygenase-2 in hyperplastic gastritis induced by Helicobacter pylori infection in C57BL/6 mice. *Aliment Pharmacol Ther*. 2001;15(6):875–886. doi:10.1046/j.1365-2036.2001.00965.x
53. Henrique Silva A, Lima Jr E, Vasquez Mansilla M, et al. A physiologically based pharmacokinetic model to predict the superparamagnetic iron oxide nanoparticles (SPIONs) accumulation in vivo. *Eur J Nanomed*. 2017;9(2):79. doi:10.1515/ejnm-2017-0001
54. Pham BTT, Colvin EK, Pham NTH, et al. Biodistribution and clearance of stable superparamagnetic maghemite iron oxide nanoparticles in mice following intraperitoneal administration. *Int J Mol Sci*. 2018;19(1):205. doi:10.3390/ijms19010205
55. Yu Q, Xiong XQ, Zhao L, et al. Biodistribution and toxicity assessment of superparamagnetic iron oxide nanoparticles in vitro and in vivo. *Curr Med Sci*. 2018;38(6):1096–1102. doi:10.1007/s11596-018-1989-8
56. Han X, Xu K, Taratula O, Farsad K. Applications of nanoparticles in biomedical imaging. *Nanoscale*. 2019;11(3):799–819. doi:10.1039/C8NR07769J
57. Shevtsov MA, Multhoff G. *Targeted and Theranostic Applications for Nanotechnologies in Medicine: Nanoparticles for Brain Tumor Targeting*. Elsevier; 2017; 487–511.
58. Vangijzegem T, Stanicki D, Laurent S. Magnetic iron oxide nanoparticles for drug delivery: applications and characteristics. *Expert Opin Drug Deliv*. 2019;16(1):69–78. doi:10.1080/17425247.2019.1554647
59. Chi JL, Li CC, Xia CQ, et al. Effect of 131 I gelatin microspheres on hepatocellular carcinoma in nude mice and its distribution after intratumoral injection. *Radiat Res*. 2014;181(4):416–424, 419. doi:10.1667/RR13539.1
60. Liu H, Xu H, Wang Y, He Z, Li S. Effect of intratumoral injection on the biodistribution and therapeutic potential of novel chemophor EL-modified single-walled nanotube loading doxorubicin. *Drug Dev Ind Pharm*. 2012;38(9):1031–1038. doi:10.3109/03639045.2011.637050
61. Xie H, Goins B, Bao A, Wang ZJ, Phillips WT. Effect of intratumoral administration on biodistribution of 64Cu-labeled nanoshells. *Int J Nanomedicine*. 2012;7:2227–2238. doi:10.2147/IJN.S30699
62. Raue A, Schilling M, Bachmann J, et al. Lessons learned from quantitative dynamical modeling in systems biology. *PLoS One*. 2013;8(9):e74335. doi:10.1371/journal.pone.0074335
63. Gogoi M, Jaiswal MK, Sarma HD, Bahadur D, Banerjee R. Biocompatibility and therapeutic evaluation of magnetic liposomes designed for self-controlled cancer hyperthermia and chemotherapy. *Integr Biol (Camb)*. 2017;9(6):555–565. doi:10.1039/C6IB00234J

64. Li Y, Sun Y, Cao T, et al. A cation-exchange controlled core-shell MnS@Bi2S3 theranostic platform for multimodal imaging guided radiation therapy with hyperthermia boost. *Nanoscale*. 2017;9(38):14364–14375. doi:10.1039/C7NR02384G
65. Liu Q, Li R, Zhu Z, et al. Enhanced antitumor efficacy, biodistribution and penetration of docetaxel-loaded biodegradable nanoparticles. *Int J Pharm*. 2012;430(1–2):350–358. doi:10.1016/j.ijpharm.2012.04.008
66. Nguyen HT, Tran TH, Thapa RK, et al. Incorporation of chemotherapeutic agent and photosensitizer in a low temperature-sensitive liposome for effective chemo-hyperthermic anticancer activity. *Expert Opin Drug Deliv*. 2017;14(2):155–164. doi:10.1080/17425247.2017.1266330
67. Wang Y, Xu H, Liu H, Wang Y, Sun J, He Z. Efficacy and biodistribution of tocopheryl polyethylene glycol succinate noncovalent functionalized single walled nanotubes loading doxorubicin in sarcoma bearing mouse model. *J Biomed Nanotechnol*. 2012;8(3):450–457. doi:10.1166/jbn.2012.1390
68. Ernsting MJ, Murakami M, Roy A, Li SD. Factors controlling the pharmacokinetics, biodistribution and intratumoral penetration of nanoparticles. *J Control Release*. 2013;172(3):782–794. doi:10.1016/j.jconrel.2013.09.013
69. Dong Q, Yang H, Wan C, et al. Her2-functionalized gold-nanoshelled magnetic hybrid nanoparticles: a theranostic agent for dual-modal imaging and photothermal therapy of breast cancer. *Nanoscale Res Lett*. 2019;14(1):235. doi:10.1186/s11671-019-3053-4
70. Shevtsov MA, Nikolaev BP, Ryzhov VA, et al. Ionizing radiation improves glioma-specific targeting of superparamagnetic iron oxide nanoparticles conjugated with cmHsp70.1 monoclonal antibodies (SPION-cmHsp70.1). *Nanoscale*. 2015;7(48):20652–20664. doi:10.1039/C5NR06521F